Photonic Spin Lattices: Symmetry Constraints for Skyrmion and Meron Topologies

Xinrui Lei,[1,2,*] Aiping Yang,[1,*] Peng Shi,[1] Zhenwei Xie,[1] Luping Du,[1,†]
Anatoly V. Zayats,[2,‡] and Xiaocong Yuan[1,§]

[1]*Nanophotonics Research Centre, Shenzhen Key Laboratory of Micro-Scale Optical Information Technology, Shenzhen University, Shenzhen 518060, China*

[2]*Department of Physics and London Centre for Nanotechnology, King's College London, Strand, London WC2R 2LS, United Kingdom*

(Received 29 July 2021; accepted 2 November 2021; published 3 December 2021)

Symmetry and topology govern many electronic, magnetic, and photonic phenomena in condensed matter physics and optics, resulting in counterintuitive skyrmion, meron, and other phenomena important for modern technologies. Here we demonstrate photonic spin lattices as a new topological construct governed by the spin-orbit coupling in an optical field. The symmetry of the electromagnetic field in the presence of the spin-orbit interaction may result in only two types of photonic spin lattices: either hexagonal spin-skyrmion or square spin-meron lattices. We show that these spin structures correspond to the lowest energy of the electromagnetic field configuration, therefore, energetically stable. We further show that in the absence of spin-orbit coupling these spin topologies are degenerated in dynamic field skyrmions, unifying the description of electromagnetic field topologies. The results provide a new understanding of electromagnetic field topology and its transformations as well as new opportunities for applications in quantum technologies, spin optics, and topological photonics.

DOI: 10.1103/PhysRevLett.127.237403

Topologically nontrivial spin textures appear in various fields from high-energy to condensed matter physics [1–5], and skyrmions [6–8] and merons [9–11] in magnetic materials are their prominent examples. Magnetic skyrmions and merons are topologically protected nanoparticlelike objects with a magnetization swirl in chiral or noncentrosymmetric magnets, important for practical applications in spintronics [6–10]. Depending on the properties of ferromagnetic materials and/or external magnetic fields, skyrmions, having integer topological number, can exist as isolated entities or condense into a lattice. In contrast to skyrmions, merons are topological constructs with a half-integer topological charge. Because of this, the individual merons cannot be observed and magnetic merons always form a lattice [10,11].

Recently, photonic analogies of magnetic skyrmions were observed in different realizations with either optical spin forming a skyrmionlike topology (photonic spin-skyrmions) [12], or a lattice of the electric field textures with hedgehog structure (photonic field skyrmions, which are dynamic field textures with the electric field oscillating in time) [13,14]. Higher order skyrmionic structures were also suggested in polarization textures [15,16]. Individual photonic spin skyrmions have been recently demonstrated using spin-orbit coupling in the evanescent field [17] to achieve topological protection through the generalized photonic quantum spin-Hall effect [18], which leads to the locking of the spin to the local momentum of the evanescent wave [19,20]. The interference of the evanescent electromagnetic fields in the sixfold symmetry cavity results in the creation of the field skyrmions in a hexagonal lattice [13,14,21]. Until now, there were no reports of photonic analogies of other spin lattices, such as spin skyrmion and spin or field merons.

Here we show that it is the symmetry of the field that completely determines the topology of the electromagnetic field of the guided modes (the modes with the evanescent field component) through spin-orbit coupling. We demonstrate both experimentally and theoretically the spin-skyrmion and spin-meron lattices formed due to a broken rotational symmetry of the field, with sixfold symmetry being responsible for a skyrmion lattice and fourfold symmetry for a meron lattice. In the absence of spin-orbit coupling (in the case when the field is not carrying topological charge), instead of spin-skyrmions, field skyrmions are formed, thus connecting two types of skyrmion manifestation in optics. We also show that the spin skyrmion and spin meron textures correspond to the lowest energy of the electromagnetic field configuration, therefore, energetically stable. The demonstrated photonic spin topologies open up new pathways for topological photonics, quantum photonics, and metrology, and a new avenue to understand topological condensed matter systems [22].

Individual photonic spin skyrmions formed due to the spin-orbit coupling in the guided waves with the evanescent field component [Fig. 1(a)] can be described by a Hertz vector potential with a helical phase term in the cylindrical coordinate (r, φ, z) as [23]

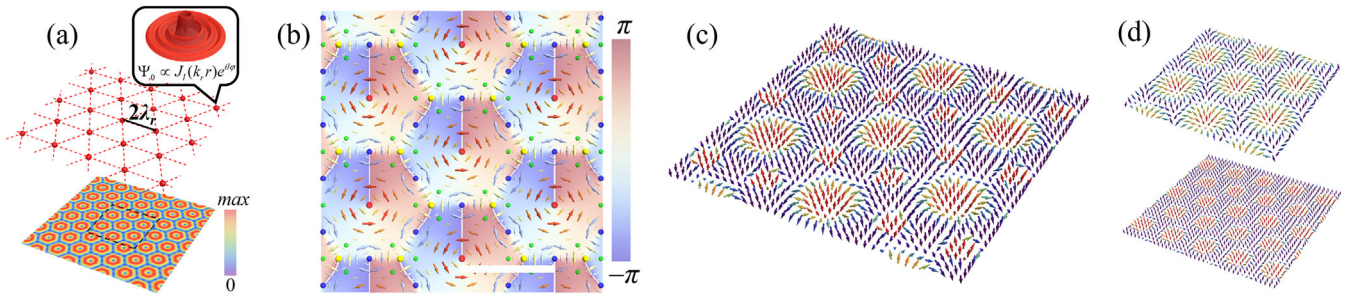

FIG. 1. (a) Schematic of the eOV lattice of hexagonal symmetry with a lattice constant $2\lambda_r$ (λ_r is in-plane wavelength) and the distribution of the amplitudes of the resultant Hertz potential. Each lattice point (red dots) is fed with an eOV described by a helical Hertz potential Ψ_0 corresponding to isolated spin-skyrmion (inset). (b) Poynting vector direction (arrows) and magnitude (arrow colors) in the generated optical vortex lattice in (a) with background color representing the phase distribution of the total Hertz potential. Red and yellow dots denote the center of the anticlockwise Poynting vector vortices in two sublattices, where the phase of the Hertz potential is singular; blue dots denote the center of clockwise ones. Green dots show the junction of different Poynting vector vortices where $P = 0$ with nonzero Hertz potential. The scale bar is λ_r. Note that the thin vertical line in each vortex is an artifact of the color representation where the phase is the same on both sides. (c) Optical spin orientation distribution corresponding to the lattice in (a) and (b) showing a spin-skyrmion lattice. The arrows indicate the direction of a unit spin vector. (d) Two sublattices of the skyrmion lattice forming the spin distribution in (c). The central "up" state in each subset can be referred to the red and yellow dots in (b), respectively.

$$\Psi_0 = AJ_l(k_r r)e^{il\varphi}e^{-k_z z}, \tag{1}$$

where A is a constant, k_r and ik_z are the transverse and longitudinal wave-vector components satisfying $k_r^2 - k_z^2 = k^2$ with k being the wave vector, and J_l is the Bessel function of the first kind of order l. The Néel-type photonic spin skyrmions are formed for $l \neq 0$, with the spin-up or -down in the center of the skyrmion, determined by the sign of l. Equation (1) describes an evanescent optical vortex (eOV) in a source free, homogeneous, and isotropic medium. If the rotational symmetry of the field is broken, individual eOVs will interact and may condense in a lattice. In order to reveal the topological features under different types of symmetry, we consider superpositions of the individual Hertz vector potentials with each lattice point fed by an eOV: $\Psi = \Psi_0 * \sum \delta(\mathbf{r} - \mathbf{r}_{mn})$, where $\mathbf{r}_{mn}$ is the position of each lattice point, δ is the Dirac delta function, and $*$ represents the operation of convolution. In two dimensions, only two Bravais lattices exist with equal lattice constants corresponding to point groups D_6 and D_4 having hexagonal and square lattices, respectively [Figs. 1(a) and 2(a)]. In view of translational and rotational symmetry imposed by a lattice, the total Hertz potential can be obtained as [24]

$$\Psi = A\sum_{n=1}^{2N} e^{il\theta_n}e^{ik_r \mathbf{r}\cdot\mathbf{e}_n}e^{-k_z z}, \tag{2}$$

where $\theta_n = n\pi/N$, $\mathbf{e}_n = (\cos\theta_n, \sin\theta_n)$ with $N = 3$ for hexagonal and $N = 2$ for square lattice. The Hertz potential in Eq. (2) exhibits rotational periodicity with total angular momentum l (we consider $l = 1$ in the following). The amplitude distributions of the Hertz potential reveal the lattice symmetry features [Figs. 1(a) and 2(a)] with zero points corresponding the singularities of the phase distribution [Figs. 1(b) and 2(b)].

The Poynting vector $\mathbf{P} = \mathrm{Re}(\mathbf{E}^* \times \mathbf{H})/2$, which represents a directional energy flux of an electromagnetic field in the lattice, can be calculated through the Hertz potential as [24]

$$\mathbf{P} = \frac{\omega\varepsilon k_r^2}{2}\mathrm{Im}(\Psi^*\nabla\Psi) \sim \langle\Psi|i\nabla|\Psi\rangle, \tag{3}$$

where ω is the angular frequency of the wave and ε is the absolute permittivity of the medium. The spin texture of the electromagnetic field can be obtained considering the Poynting vector distribution in the lattice since for TM/TE polarized evanescent waves, the intrinsic spin-momentum coupling yields a relationship between the SAM $\mathbf{S}$ and the Poynting vector $\mathbf{P}$ as [19]

$$\mathbf{S} = \frac{1}{2\omega^2}\nabla \times \mathbf{P}. \tag{4}$$

The generalized spin-momentum relationship in Eq. (4) is a manifestation of the conservation law of SAM, which indicates that the SAM of an evanescent field originates from the vortices of the electromagnetic energy flow. Equation (4) can be expressed in terms of the Hertz potential as $\mathbf{S} = (\varepsilon k_r^2/4\omega)\mathrm{Im}(\nabla\Psi^* \times \nabla\Psi) \sim \langle\nabla\Psi| \times i|\nabla\Psi\rangle$, revealing that the SAM of an evanescent field is in correspondence to the Berry curvature of the Hertz potential [25]. Consequently, a nontrivial spin texture is a consequence of winding of the Hertz potential in the presence of spin-orbit coupling (e.g., formation of an individual spin skyrmion as $l \neq 0$).

The phase singularity of the Hertz potential pins the center of each Poynting vector vortex [Eq. (3)] and,

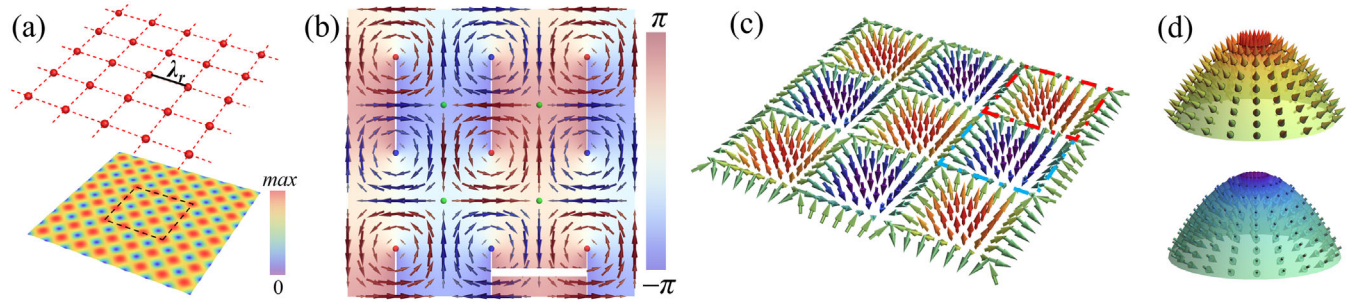

FIG. 2. (a) Schematic and the distribution of the Hertz potential amplitude for the evanescent optical vortex lattice of square symmetry with a lattice constant λ_r. (b) Poynting vector direction (arrows) and magnitude (arrow colors) for the square lattice in (a). The scale bar is $\lambda_r/2$. (c) Optical spin orientation distribution corresponding to the lattice in (a) and (b). The dashed red and blue squares indicate unit cells of the spin-meron lattice with skyrmion number $Q = \pm ½$, which can be smoothly mapped on a paraboloid in (d).

depending on the symmetry of the lattice, the in-plane Poynting vector forms different types of vortex distributions. For a hexagonal lattice, the Poynting vector distribution has a rotational symmetry with a characteristic angle of $\pi/3$ as $\hat{R}(\pi/3)\mathbf{P}(\mathbf{r}) = \mathbf{P}[\hat{R}(\pi/3)\mathbf{r}]$, where $\hat{R}(\theta)$ is the rotation matrix along z axis. A hierarchical structure of the Poynting vector vortices is obtained with two sublattices, due to the multiple vortex centers in each unit cell of the lattice [Fig. 1(b)], which can be considered as an optical analogue of the Abrikosov vortex lattice [26]. The appearance of two subsets of the Poynting vector vortex lattice can be attributed to the different compositions of the wave numbers [24]. While for a square lattice, the Poynting vector distribution has a rotational symmetry of $\pi/2$ as $\hat{R}(\pi/2)\mathbf{P}(\mathbf{r}) = \mathbf{P}[\hat{R}(\pi/2)\mathbf{r}]$. The energy flow in each unit cell exhibits a vortex with winding number ± 1 [Fig. 2(b)], which is an optical analogue of the so-called staggered flux in condensed matter systems [27,28]. The junction of the vortices in Figs. 1(b) and 2(b) can be found where the Poynting vector is zero but the Hertz potential is nonzero.

These two types of vortices in the Poynting vector distributions determine the topology of the spin textures. The topological invariant Q, which is known as the skyrmion number, can be obtained as $Q = (1/4\pi)\iint \mathbf{n} \cdot (\partial_x \mathbf{n} \times \partial_y \mathbf{n}) dxdy$, where $\mathbf{n} = \mathbf{S}/|\mathbf{S}|$ represents the unit vector in the direction of a three-component spin. Since each vortex center of the Poynting vector is the phase singularity of the Hertz vector, where the Poynting vector is zero, only the z component of the SAM is present in the center of the vortex [Eq. (4)], with sign of S_z determined by the rotation direction of the Poynting vector vortex. For a hexagonal lattice, two skyrmion sublattices are observed, according to the structure of the Poynting vector distribution, with skyrmion number $Q = 1$ for each unit cell of the sublattice where the spin vectors vary progressively from the central "up" state to the edge "down" state, manifesting a Néel-type photonic spin-skyrmion [Figs. 1(c) and 1(d)] without increased spin flux. For other angular momenta with nonzero SAM ($l = 2, 4, 5$), the two skyrmion sublattices will emerge with different signs of skyrmion numbers, demonstrating four realizations of spin-skyrmion topology [24].

On the other hand, the staggered-flux configuration of the Poynting vector observed in a square lattice gives rise to the formation of a photonics spin-meron lattice. From Eq. (4), the SAM distribution can be obtained as $\mathbf{S} \propto [k_z \sin(k_r x)\cos(k_r y), k_z \cos(k_r x)\sin(k_r y), k_r \cos(k_r x) \times \cos(k_r y)]$, which possesses distinct domains where the z component of the local spin orientation goes to zero and merons are confined in a unit cell [Fig. 2(c)]. In each unit cell, the spin vector tilts progressively from the central "up" or "down" state to the edge where z component of SAM $S_z = 0$. The skyrmion number calculated for each unit cell in the spin texture is $Q = \pm ½$, corresponding to the Néel-type photonic "core-up" or "core-down" spin-meron topology with a nonzero spin flux [24]. These spin configurations in each unit cell can be smoothly mapped on a paraboloid $z = -r^2/2$ by converting the in-plane spin vector to an infinite circle with substitution $(k_z/k_r)\tan(k_r x) = r\cos\varphi$ and $(k_z/k_r)\tan(k_r y) = r\sin\varphi$ [Fig. 2(d)]. Similar spin configurations can be obtained for $l = 3$ with opposite signs of skyrmion numbers in each unit cell [24]. The obtained square spin-meron lattice with alternating Poynting vector vorticities is in analogy with the lowest-energy multimeron configuration in frustrated magnets [29,30].

It is worth noting that in the case of $l = 0$, the SAM vanishes and, in the absence of spin-orbit coupling, the spin skyrmion and meron are not present. In this case, the considered sixfold and fourfold symmetry lattices of the Hertz potential result in the oscillating electric field patterns which exhibit field topologies corresponding to a field-skyrmion lattice for D_6 and a field-meron lattice for D_4 symmetry [24] (see Fig. S1 in the Supplemental Material [24]). This provides connection between the concepts of spin skyrmions formed due to the spin-orbit coupling [12] and dynamic, time-dependent field skyrmions formed due to the interference effects [13,14].

The configuration of a square meron lattice can be understood from the thermodynamic perspective considering the

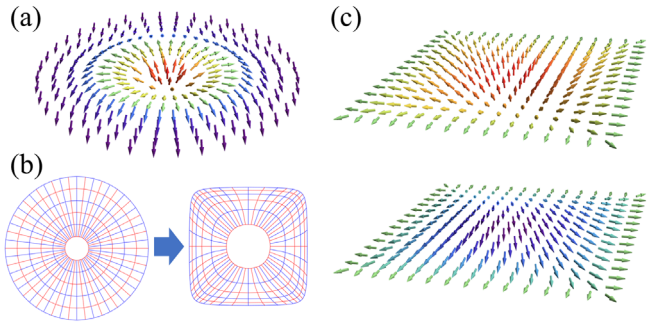

FIG. 3. (a) Isolated skyrmion configuration in a cylindrical system derived from the lowest energy theorem in the nonlinear sigma model. (b) Coordinate transformation from an infinite circle to a confined square when a square spin lattice is formed. (c) Two meron configurations confined in a square corresponding to two solutions of Eq. (5) with $Q = \pm 1/2$, forming the spin lattice in Fig. 2(c).

lowest-energy theorem. For magnetic skyrmions, the energy Hamiltonian is given by the nonlinear sigma model together with the Dzyaloshinskii-Moriya interactions for the antisymmetric exchange between two neighboring magnetic spins [8,31]. A meron lattice can be stabilized in chiral magnets with anisotropy [32,33]. Considering the generalized photonic quantum spin-Hall effect for transverse spin which reveals an analogy between photonic and electron spin [18], the energy for a photonic skyrmion texture is described by the Hamiltonian in the classical nonlinear sigma model [34]

$$H = \frac{1}{2}\int (\nabla \mathbf{n})^2 dxdy, \tag{5}$$

where $\mathbf{n}$ represents the unit spin vector. The individual spin-skyrmion solution can be obtained in the system with the rotational symmetry as $\theta(r) = 2\arctan(r)$ by using the Euler-Lagrange equation for the lowest energy [24] and applying boundary conditions $n_z(0) = 1$ at the core and $n_z(\infty) = -1$ at infinity [Fig. 3(a)]. If we chose the boundary conditions corresponding to a square spin lattice: $n_z(0) = \pm 1$ at the core and $n_z(\infty) = 0$ at the edge of the unit cell [Fig. 3(b)], the exact numerical solution for a meron state can be obtained behaving as $\theta(r) \approx \arctan(r)$ or $\theta(r) \approx \pi - \arctan(r)$ [Fig. 3(c)]. These solutions correspond to the SAM configuration of a square lattice in Fig. 2(c) (Ref. [24]). It was not possible to find an analytical solution to Eq. (5) for a skyrmion lattice because of the difficulties with defining boundary conditions due to the composite sublattice structure.

We experimentally demonstrated the spin lattices of the evanescent vortex beams on the example of surface plasmon polaritons (SPPs) sustained at a dielectric-metal interface [35]. A radially polarized laser beam with helical wavefront (topological charge $l = 1$, wavelength $\lambda = 532$ nm) is tightly focused onto a thin silver film surface, which provides an excitation of SPPs with OAM at air-silver interface. Under such conditions, individual photonic spin

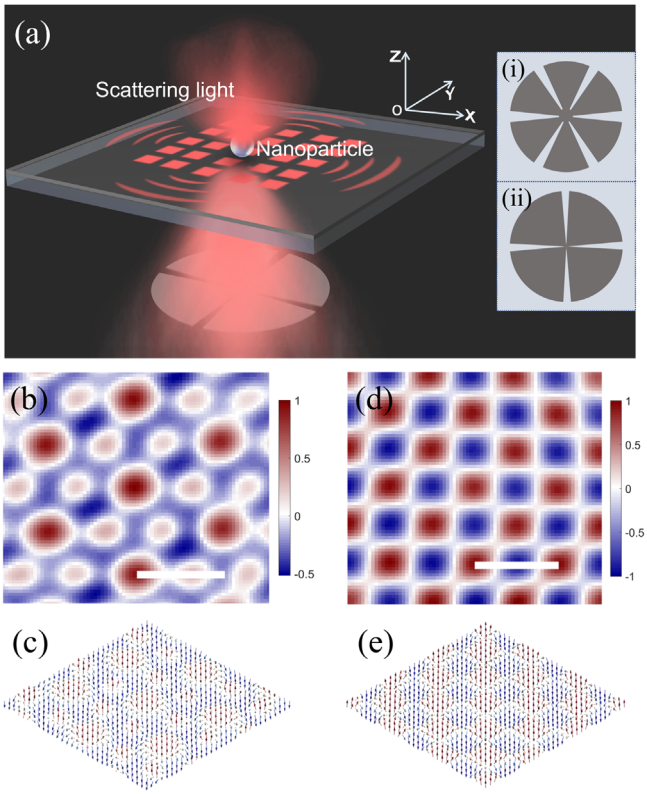

FIG. 4. (a) Schematic diagram of the experiment. SPPs are excited on a surface of a thin silver film by a tightly focused, radially polarized beam modulated by the intensity masks comprised of sixfold or fourfold symmetry apertures. A dielectric nanosphere is employed as a near-field probe to characterize the spin texture of the spin lattice, formed at the center area induced by the spin-orbit interaction in SPPs. (b)–(e) Measured S_z component (b),(d) and local spin orientation (c),(e) in the lattice obtained with the field of sixfold (b),(c) and fourfold (d),(e) symmetry. The scale bar in (b) and (d) is the SPP wavelength. In (c) and (e), the arrows indicate the orientation of the normalized spin vectors, with the z direction color coded to the same color scale as (b) and (d).

skyrmions are formed on the metal interface in the case if rotational symmetry is not broken [12]. To break the rotational symmetry, the incident beam was modulated with intensity masks comprised of either sixfold or fourfold symmetry apertures. The spin-skyrmion or spin-meron textures are formed in the case of sixfold or fourfold symmetry, respectively, due to interference of the SPPs in the presence of the spin-orbit interaction [Fig. 4(a)]. A spin-resolved near-field scanning optical microscope was used with a dielectric nanosphere as a near-field probe to characterize the spin texture of the vortex lattice [36] (see Ref. [24] for the details of the experiment). The measured S_z distributions and the retrieved local spin vector orientation exhibit a skyrmion-type lattice for the field of sixfold symmetry and reveal spin-meron lattice for fourfold symmetry [Figs. 4(b)–4(e)]. These distributions correspond well to the simulation results for respective symmetries of the plasmonic field

[cf. Figs. 4(c), 4(e) and 2(c), 3(c)], revealing two interleaved skyrmion sublattices for a hexagonal lattice and square lattice of positive or negative merons.

In conclusion, we demonstrated the formation of photonic spin-skyrmion and spin-meron lattices in real space based on spin-orbit coupling in the evanescent waves in the environment with broken rotational symmetry. We showed that the field symmetry is the key for determining the photonic spin topology, resulting in either sixfold symmetry spin-skyrmion lattices or fourfold symmetry of spin-meron lattices. These two kinds of spin-lattice topologies were verified on the example of SPP waves in the presence of spin-orbit coupling in the broken rotational symmetry conditions. In the absence of spin-orbit coupling, the spin lattices are degenerated to time-dependent field-skyrmion or field-meron lattices. Thermodynamic considerations confirm stability of spin-textures of the evanescence waves. These new topological features of electromagnetic waves may provide new insights on the properties of skyrmion and meron topological structures and their transformations in condensed matter physics, where they may be difficult to realize, as well as new applications in metrology (e.g., for magnetic domain observations [37]), topological and quantum photonics, and spin optics.

This research was supported by the Guangdong Major Project of Basic Research No. 2020B0301030009, National Natural Science Foundation of China Grants No. U1701661, No. 61935013, No. 62075139, No. 61622504, No. 61705135 and No. 61905163, the leadership of Guangdong province program Grant No. 00201505, the Natural Science Foundation of Guangdong Province Grant No. 2016A030312010, the Shenzhen Peacock Plan KQTD20170330110444030 and KQTD2015071016560101, the Science and Technology Innovation Commission of Shenzhen Grants RCJC20200714114435063 and JCYJ20200109114018750, the EPSRC (UK), and the ERC iCOMM project (789340). L. D. acknowledges the support given by the Guangdong Special Support Program. All the data supporting the findings of this study are available in the main text and Supplemental Material [24].

*These authors contributed equally to this work.
†Corresponding author.
lpdu@szu.edu.cn
‡Corresponding author.
a.zayats@kcl.ac.uk
§Corresponding author.
xcyuan@szu.edu.cn

[1] D. Hsieh *et al.*, Science **323**, 919 (2009).
[2] M. R. Matthews, B. P. Anderson, P. C. Haljan, D. S. Hall, C. E. Wieman, and E. A. Cornell, Phys. Rev. Lett. **83**, 2498 (1999).
[3] L. Lu, J. D. Joannopoulos, and M. Soljačić, Nat. Photonics **8**, 821 (2014).
[4] D. Hsieh, D. Qian, L. Wray, Y. Xia, Y. S. Hor, R. J. Cava, and M. Z. Hasan, Nature (London) **452**, 970 (2008).
[5] J. E. Moore, Nature (London) **464**, 194 (2010).
[6] N. Nagaosa and Y. Tokura, Nat. Nanotechnol. **8**, 899 (2013).
[7] A. Fert, N. Reyren, and V. Cros, Nat. Rev. Mater. **2**, 17031 (2017).
[8] S. Mühlbauer, Science **323**, 915 (2009).
[9] N. Gao *et al.*, Nat. Commun. **10**, 5603 (2019).
[10] X. Z. Yu, W. Koshibae, Y. Tokunaga, K. Shibata, Y. Taguchi, N. Nagaosa, and Y. Tokura, Nature (London) **564**, 95 (2018).
[11] K. Moon, H. Mori, K. Yang, S. M. Girvin, A. H. MacDonald, L. Zheng, D. Yoshioka, and S.-C. Zhang, Phys. Rev. B **51**, 5138 (1995).
[12] L. Du, A. Yang, A. V. Zayats, and X. Yuan, Nat. Phys. **15**, 650 (2019).
[13] S. Tsesses, E. Ostrovsky, K. Cohen, B. Gjonaj, N. H. Lindner, and G. Bartal, Science **361**, 993 (2018).
[14] T. J. Davis *et al.*, Science **368**, eaba6415 (2020).
[15] M. Król *et al.*, Optica **8**, 255 (2021).
[16] W. Lin, Y. Ota, Y. Arakawa, and S. Iwamoto, Phys. Rev. Research **3**, 023055 (2021).
[17] K. Y. Bliokh, F. J. Rodríguez-Fortuño, F. Nori, and A. V. Zayats, Nat. Photonics **9**, 796 (2015).
[18] K. Y. Bliokh, D. Smirnova, and F. Nori, Science **348**, 1448 (2015).
[19] P. Shi *et al.*, Proc. Natl. Acad. Sci. U.S.A. **118**, e2018816118 (2021).
[20] T. Van Mechelen and Z. Jacob, Opt. Mater. Express **9**, 95 (2019).
[21] S. Tsesses, K. Cohen, E. Ostrovsky, B. Gjonaj, and G. Bartal, Nano Lett. **19**, 4010 (2019).
[22] T. Van Mechelen, W. Sun, and Z. Jacob, Nat. Commun. **12**, 4729 (2021).
[23] A. Ishimaru, *Electromagnetic Wave Propagation, Radiation, and Scattering from Fundamentals to Applications* (Wiley, New York, 2017).
[24] See Supplemental Material at http://link.aps.org/supplemental/10.1103/PhysRevLett.127.237403 for eigenmode analysis of the Helmholtz equation with sixfold and fourfold symmetry; analysis of the Poynting vector vortices with different symmetries; skyrmion feature with different symmetries; coupling and transition between SAM and Poynting vector; energy considerations for a spin-meron lattice configuration; experimental setup for exciting and measuring the photonic spin lattices; Figs. S1–S5.
[25] D. Xiao, M.-C. Chang, and Q. Niu, Rev. Mod. Phys. **82**, 1959 (2010).
[26] B. Rosenstein and D. Li, Rev. Mod. Phys. **82**, 109 (2010).
[27] C. C. Chang and R. T. Scalettar, Phys. Rev. Lett. **109**, 026404 (2012).
[28] L. K. Lim, C. M. Smith, and A. Hemmerich, Phys. Rev. Lett. **100**, 130402 (2008).
[29] Y. A. Kharkov, O. P. Sushkov, and M. Mostovoy, Phys. Rev. Lett. **119**, 207201 (2017).

[30] U. K. Rossler, A. N. Bogdanov, and C. Pfleiderer, Nature (London) **442**, 797 (2006).
[31] X. Z. Yu, Y. Onose, N. Kanazawa, J. H. Park, J. H. Han, Y. Matsui, N. Nagaosa, and Y. Tokura, Nature (London) **465**, 901 (2010).
[32] S.-Z. Lin, A. Saxena, and C. D. Batista, Phys. Rev. B **91**, 224407 (2015).
[33] M. Ezawa, Phys. Rev. B **83**, 100408 (2011).
[34] R. Rajaraman, *Solitons and Instantons* (North-Holland, Amsterdam, 1982).
[35] A. V. Zayats, I. I. Smolyaninov, and A. A. Maradudin, Phys. Rep. **408**, 131 (2005).
[36] C. Li, P. Shi, L. Du, and X. Yuan, Nanoscale **12**, 13674 (2020).
[37] X. Lei, L. Du, X. Yuan, and A. V. Zayats, Nanophotonics **10**, 3667 (2021).